

## Detection of Bone Tumor from Histopathological Images Using Aquila optimizer based feature extraction and VGG-19+RESNET50 Classifier

<sup>1</sup> D. Anand, <sup>2</sup> G. Arulselvi, <sup>3</sup>G.N. Balaji

<sup>1</sup> Research Scholar, Department of Computer science and Engineering, FEAT, Annamalai University, Chidambaram.

<sup>1</sup>Department of CSE, Koneru Lakshmaiah Education Foundation, Vaddeswaram, AP, India.

<sup>2</sup>Department of Computer Science and Engineering, FEAT, Annamalai University, Chidambaram.

<sup>3</sup> School of Computer Science and Engineering, Vellore Institute of Technology, Vellore.

Email id: <sup>1</sup>ananddama92@gmail.com, <sup>2</sup>arulselvidhanasekaran@gmail.com,

<sup>3</sup>balaji.gnb@gmail.com

### Abstract

Primary bone tumours are the cause of new paediatric cancer cases globally. Osteosarcoma is the most prevalent kind of malignant bone tumour. The objective of the present effort is to increase the accuracy of computer-aided detection (CAD) and diagnosis in the identification and treatment of osteosarcoma. Convolutional neural networks (CNNs) are a technique that may considerably reduce the workload of the surgeon and improve patient prognosis. For CNNs to function more reliably, a lot of data must be used throughout the training process. In order to distinguish necrotic pictures from non-necrotic and healthy tissues, transfer learning methods using pre-trained CNNs are used to a public dataset of osteosarcoma histology images. In this research, the first step in preprocessing is utilising the histogram approach to decrease the noise in the images. Utilizing the Aquila optimizer architecture, preparatory pictures are retrieved to increase the accuracy of identifying anomalous parts surrounding the afflicted area. Then, using VGG-19+RESNET50, categorise the precise spotting and rank the bone tissue as normal and pathological. Our refined model showed state-of-the-art performance in identifying Osteosarcoma malignancy from histologic pictures. The suggested VGG-19+RESNET50 classifier is discovered to obtain 99.7% accuracy, 98.9% precision, 99.2% recall, and 99.3% F1-score.

### Introduction

The most prevalent main peripheral osseous, lung cancer is osteosarcoma [1]. Neo-adjuvant chemotherapy and surgery are current therapeutic modalities that have improved patient survival rates by nearly five years. Between 1975 and 2010 [2], the five-year mortality rate for osteosarcoma patients improved from 40% to 76% for children under 15 years old and from 56% to 66% people between 15 and 19 years old. Still, less than 20% of patients with metastatic osteosarcoma survive five years [3]. The overall survival rate may be increased by early diagnosis of osteosarcoma and diligent monitoring throughout the treatment phase [4]. However, the survival rate is substantially lower in developing nations like Bangladesh because to a shortage of radiologists. Furthermore, evaluating the grade of osteosarcoma cancer and necrosis cells throughout the treatment phase required at least two or more radiologists to perform a quantitative analysis of medical images [5]. Our objective is to develop a model that can be applied to smart hospital management systems and telemedicine in order to facilitate expert diagnosis. It is time-consuming and occasionally inaccurate to manually inspect or use image processing technology to analyse prior histopathological images to identify nuclei clusters, nuclei sizes, etc. [6]. However, modern artificial intelligence (AI) algorithms are being used to quickly identify the characteristic in complicated datasets for cancer cell identification. Additionally, using AI to diagnose the symptoms may aid patients and doctors more effectively [7]. Additionally, the application of AI in the area of histology has prepared the road for improved cancer diagnosis, classification, and detection. As a consequence, WSIs are currently preferred by researchers over CT and MRI scans for the accurate diagnosis of osteosarcomas. Hematoxylin and eosin staining tissue samples from the afflicted areas is one of the most used techniques for detecting these cells [8]. A pathologist will examine the samples under a

microscope after staining and mounting them on glass slides. Whole slide images (WSIs), that are unprocessed digital reproductions of glass slides, were used in this research. The process of feature extraction in automatic detection systems is the next step, and it may be done manually or using deep learning (DL). By lowering the dimensionality of incoming data, a process called as feature extraction, data are displayed and interpreted effectively [10]. These techniques are often used to extract handcrafted (HC) features, which are picture-specific attributes created by hand based on the characteristics of the targeted region. HC characteristics are widely used by researchers because they are simple to extract, especially from small datasets. With the assistance of experts in the relevant field, the features may be ascertained [11]. These characteristics are complicated, making it challenging to distinguish them from complex pictures. Deep learning models (DLMs) are used here as a feature extraction method. In the last ten years, DLMs have acquired a lot of momentum due to recent advancements in processing, such as the introduction of faster and more compact processors, which have made it possible for experts to train deeper networks rapidly and easily [12]. In this instance, a convolutional neural network is often employed as the DLM for the feature extraction (CNN). These models can automatically extract properties from a picture, but they need a large training sample with a significant amount of variation to achieve acceptable attribute derivation quality. By providing additional low-level features, one may use them to more accurately characterize a picture and improve its feature analysis [13]. Because DLM can do the same task automatically, it has the benefit of not needing any significant pre-processing. However, a disadvantage of such models is their high computational and data needs. Consequently, the following are the contributions of this research:

- To construct VGG-19+RESNET50 classifier to classify the exact spotting and to grade the bone tissue as normal and abnormal.
- A binary version of the Aquila optimizer is adopted as an feature extraction technique, which is also used to select optimal features and enhance the classification accuracy.

This paper consists of the ensuing segments: Segment 1 represents the outline of bone cancer, the function of Histopathology in cancer diagnosis, , Segment 2 exhibits the present schemes for cancer detection methods with its limitation, Segment 3 provides the feature extraction model and classification model, Segment 4 presents the productive experimental assessment, and Segment 5 sums up with a conclusion and upcoming study.

#### **Related works**

Two feature sets, one with hog and others without, are created in [14] after first determining the best applicable edge detection technique. Support vector machine (SVM) and Random forest are two machine learning models that are used to analyse the effectiveness of these selected features. Convolutional neural networks (CNN) are suggested in [15] as a technique to increase the efficiency and accuracy of classifying osteosarcoma tumours into tumour classifications (viable tumour, necrosis) against non-tumor. The proposed CNN architecture comprises five learned layers: two completely connected layers with data preprocessing approaches to increase effectiveness, and two fully connected layers with three convolutional layers separated by max pooling layers for extracting features. We discover that the classification of osteosarcoma may be done very effectively and accurately by using neural networks. Researchers develop a Convolutional Extreme Learning Machine (DC-ELM) system in [16] to identify the kind of cancer using histopathology images. This technique is a combination of five significant classifiers. In the suggested framework, we exclusively use the karhunenloeve extraction approach to extract certain picture characteristics, allowing us to distinguish between good and diseased bone areas. Developed a multitask deep learning (DL) model for the radiographic segmentation, classification, and location of primary bone cancers in [17]. All patients had their bone tumours classified as benign or malignant using the histopathologic results as the gold standard. Seventy percent of the patients were divided into the training set, fifteen percent into the validation set, and fifteen percent into the test set using split-sample validation. Use the example of osteosarcoma in [18] to highlight the drawbacks and how using model input variability might enhance model performance. We retrain an osteosarcoma classification model that was previously reported using the publicly accessible osteosarcoma dataset. In contrast to the original work, we divide the identical collection of photographs into training and testing datasets: the training dataset includes images from all patients, whereas the test dataset only includes images through one

patient. The revised partition scheme drastically reduces the effectiveness of the algorithm on the test set, which points to overfitting and a lack of model generalization. A deep-learning architecture was created and trained using the same data set in [19]. The models performed very well when we calculated the receiver-operator characteristic for differentiating between a tumour and a non-tumour, followed by conditional differentiating between a necrotic tumour and a viable tumour. The areas of interest on image-tiles created from test whole-slide pictures were then identified using the trained models. In [20], morphologic characteristics were extracted and the capacity of the algorithms to recognise pertinent morphologic patterns is shown by the correlation between mutant prediction probability and variant allele frequency and the number of impacted genes per pathway.

The fundamental element of machine learning and data mining algorithms is that training and prospective data should be distributed in the same area. The issue arises when there are insufficient training data for the given research subject. As a result, we can use pre-trained networks that have been applied to bigger data sets from other domains to gain the fundamental parameters for training our deep learning model. In these circumstances, effective information transmission while limiting costly data labelling procedures dramatically enhances learning outcomes.

**Research methodology**

The suggested method for detecting bone cancer is discussed in this section. The first step in preprocessing is utilising the histogram approach to reduce the noise in the photos. Utilizing the Aquila optimizer architecture, preparatory pictures are retrieved to increase the accuracy of identifying anomalous parts surrounding the afflicted area. Then, utilising VGG-19+RESNET50 as shown in figure 1, to categorise the precise spotting and to grade the bone tissue as normal and pathological.

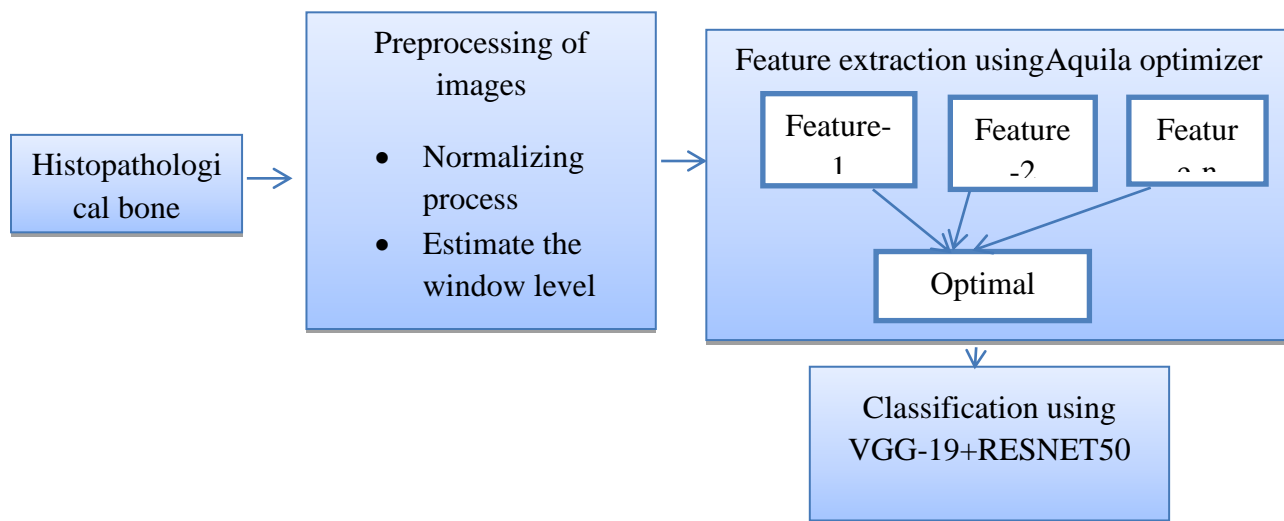


Figure-1 Overall Proposed architecture for bone cancer classification

**Dataset acquisition**

In this research, the osteosarcoma histology image dataset was utilised. The dataset is available for download from the Cancer Imaging Archive website (TCIA). A clinical scientist team from the University of Texas Southwestern Medical Center gathered the information from the patients admitted between 1995 and 2015. The dataset is openly accessible for study on the TCIA website. The collection includes 1024 X 1024 pixel Hematoxylin

and Eosin stained histological photos of osteosarcoma. Three kinds of histology photos make up the dataset: non-tumor (NT), non-viable tumour (NVT), and viable tumour (VT). The Non-Tumor class, which comprises the majority of the collection, has 536 photos showing bone, blood vessels, and cartilage in their natural states. A dataset of 263 and 345 photos, respectively, has minority classes for non-viable tumours and viable tumours. Images from the NVT class depict tissues that are either dead or in a reasonably early state of healing. In the VT area of histology pictures, nuclei are grouped together and are coloured darkly.

**Preprocessing of bone dataset**

The characteristics of the voxels from the pictures on such three planes are obtained in the histogram-based pre-processing technique, and a training dataset is built utilising these features for the classification process. Each voxel is tagged as either a tumour or non-tumor class with the suitable threshold selection for the classification results. The suggested approach is evaluated using a classifier on the suspected tumour location in each slice. Simply normalising the window level and range around the lung intensity histogram allows for the contrast modification. Furthermore, a Gabor filter is used to lower the noise level. The filtered blocks are then placed back in their original locations. Due to the overlap between these blocks, several estimations were made for each pixel. We first create an edge picture for each tumour cell and then superimpose it with two circles, L in and L out, whose centres are the same as the tumour candidate's 2D ROI and with corresponding radii of rin and rout. In Equations 1 and 2, their parameters are provided.

$$rout = 4 + \frac{L}{2}, rin = rout/2, if(L \geq 10) \tag{1}$$

And

$$rout = 2 + \frac{L}{2}, rin = \frac{rout}{2} - 1, if(L < 10) \tag{2}$$

Where,

L is the measure of the filtered image's longer side. If a tumor candidate is roughly spherical in form, the edge of the tumor is between the circles L\_in and \_out, and a significant amount of the tumour area is circumscribed by the circle L\_in.

Particularly significant for some of the darker photographs are edge characteristics. Since the training picture had a normal quality, we were able to prevent using the edge feature. However, it is used for testing on some of the darker photos in the collection. The Canny edge detection technique was used using the default threshold. Since the edge feature by itself is relatively inefficient, we must combine it with a more potent characteristic, like color. In order to characterize the outside and inner areas of bone tumors, it is paired with the color feature.

**Feature extraction using Aquila optimizer**

Following preprocessing, the Aquila optimization Technique is employed for feature extraction. A newly proposed algorithm that imitates the natural Aquila hunting process is called the Aquila optimizer (AO). The process of hunting includes four steps: extended exploration, which is performed by flying high with a vertical stoop, narrowed exploration, which is accomplished by moving with a contour flight, expanded exploiting, which is performed by low-flying descending assault, and narrowed exploiting, which is accomplished by strolling and capturing prey. To transition from the exploration stage to the exploitation stage, the AO algorithm uses a variety of behaviours. The first two-thirds of repetitions replicate the exploration stage, while the latter third of iterations represent the exploitation stage. The AO method is shown mathematically as follows.

Initializing: As its first step, the AO method applies Equation (1) to distribute N solutions throughout a predetermined range [Low, Upp] in a D-dimensional search space.

$$Y_{i,j} = Low_j + a \times (Upp_j - Low_j)$$

where  $Y_{i,j}$  is the j-th dimension of the i-th solution,  $Low_j$  and  $Upp_j$  indicates the lower and upper bound value of the j-th dimension in the search space, and  $a$  is selected at random from the range of 0 to 1.

where  $a$  is selected at random from the range of 0 to 1,  $Y_{i,j}$  represents the j-th dimension of the i-th solution,  $Low_j$  and  $Upp_j$  denote the lower and upper limit values of the j-th dimension in the search space. The matrix  $Y_{J \times K}$  maintains the location of the solutions. The fitness value of each individual solution is then determined by  $f(Y_i)$ .

Expanded exploration: An Aquila locates its prey by high-flying while descending vertically, then chooses the best hunting spot. Due to this activity, the search area is surveyed from great heights in an effort to determine where the prey could be. Equation (2) in AO simulates this behaviour, which is carried out when  $it_{er} < (2/3 \times Max_{it_{er}})$  and a randomly generated value  $< 0.5$ .

$$Y_1(it_{er} + 1) = Y_{best}(it_{er}) \times \left(1 - \frac{it_{er}}{Max_{it_{er}}}\right) + (Y_M(it_{er}) - Y_{best}(it_{er}) \times r)$$

where  $Y_{best}(it_{er})$  is the best solution obtained up to the present iteration and roughly approximates the location of the prey, and  $Y_1(it_{er} + 1)$  is the answer provided by the prime technique to utilise in the upcoming iteration.

The  $1 - \frac{it_{er}}{Max_{it_{er}}}$  term, where  $it_{er}$  stands for the present iteration and  $Max_{it_{er}}$  represents the maximum number of iterations that may be executed, is used to control the scope of the investigation depending on the number of iterations. The mean of the solutions that are now accessible, as calculated by Equation (3), is shown in the  $it_{er}$ -th iteration by  $Y_M(it_{er})$ ,

$$Y_M(it_{er}) = \frac{1}{Num_{sol}} \sum_{i=1}^N Y_i(it_{er}) \text{ where } j = 1, 2, 3 \dots L$$

where  $L$  indicates the search space's dimension, and  $Num_{sol}$  is the number of solutions.

Narrowed exploration: The second phase entails the hunting technique known as contour flying of a brief glide assault. Aquila soars above the intended prey, gets ready to dive, and strikes when it is seen from a great height. This characteristic enables the Aquila to narrowly investigate a particular region. Equation (4) in AO simulates this tendency to limit the exploration when the randomly produced value is greater than 0.5 and  $it_{er} < \left(\frac{2}{3} \times Max_{it_{er}}\right)$ .

$$Y_2(it_{er} + 1) = Y_{best}(it_{er}) \times levy(G) + Y_R(it_{er}) + (y - x) \times r$$

where accordingly,  $Y_2(it_{er} + 1)$ ,  $Y_R(it_{er})$  and  $levy(G)$  stand for the solutions generated by the narrower exploration strategy, a randomly chosen solution from all of the solutions in the  $it_{er}$ -th iteration, and the Levy flight distribution function determined by Equation (5),

$$levy(G) = a \times \frac{c \times C}{e}, C = \frac{\delta(1+\alpha) \times \sin.\frac{\pi\alpha}{2}}{\left(1 + \frac{\alpha}{2}\right) \times \alpha \times 2^{\alpha-\frac{1}{2}}}$$

where  $c$  and  $e$  are random integer integers between  $[0, 1]$ ,  $a = 0.01$ ,  $\alpha = 1.5$ . Equation (4) uses Equation (6) to determine  $y$  and  $x$ , which reflect the spiral shape,

$$y = p \times \cos(\theta), x = p \times \sin(\theta)$$

Expanded exploitation: During the extended exploitation stage, Aquila uses the third strategy to seek prey. The Aquila is ready to take flight and launch an assault after carefully locating the prey zone. The Aquila descends vertically and executes the initial strike to assess how the prey will react to the assault. When  $it_{er} > (2/3 \times Max_{it_{er}})$  and the randomly generated value produced by Equation (9) is less than 0.5, the low-flying descent assault conduct, is carried out

$$Y_3(it_{er} + 1) = (Y_{best}(it_{er}) - Y_M(it_{er})) \times \alpha - r + ((Upp - Low) \times r + L) \times \mu$$

where  $Y_3(it_{er} + 1)$  represents for the solutions acquired using the extended exploitation approach, and where the exploitation adjustment parameters  $\alpha$  and  $\mu$  and are set to 0.1.

Narrowed exploitation: When the Aquila approaches the target and randomly attacks, the fourth hunting tactic is performed during the more narrowed exploitation stage. This behavior refers walking and grabbing the prey and is completed when and randomly produced value  $> 0.5$  by Equation (10).

When  $it_{er} > (2/3 \times Max_{it_{er}})$  and a randomly generated value produced by Equation (10)  $> 0.5$ , the behavior known as "walking and seizing the prey" occurs

$$Y_4(it_{er} + 1) = AF(it_{er}) \times Y_{best}(it_{er}) - (track_1 \times Y(it_{er}) \times r) - track_2 \times levy(G) + r + track_1$$

where  $Y(it_{er})$  represents the current answer for the  $(it_{er})$ -th iteration, and  $Y_4(it_{er} + 1)$  signifies the produced fourth search solutions. In order to balance the search strategy, a quality function known as QF is determined using Equation (11).

$$AF(it_{er}) = t^{\frac{2 \times r - 1}{1 - Max_{it_{er}}}}$$

are numbers that depict the prey tracking motions of the aquila, with values ranging from 2 to 0. The calculation of are done by Equations (12) and (13)

The numbers  $track_1$  and  $track_2$  depict the motions of the Aquila's prey, with  $track_2$ 's value decreasing from 2 to 0. Equations (12) and (13) are used to calculate  $track_1$  and  $track_2$ ,

$$track_1 = 2 \times r - 1$$

$$track_2 = 2 \times \left(1 - \frac{it_{er}}{Max_{it_{er}}}\right)$$

In order to increase classification performance, minimise computing cost, and promote learning capabilities, relevant features in a dataset must be found. Depending on the nature of the feature selection issue, a binary method is used to choose the best feature subset. The binary technique uses binary vectors with D entries to represent each solution, where D is the number of features in the dataset. The values of each element in the solution vector are 0 or 1, with 0 indicating no selection and 1 denoting the selection of that specific characteristic. Two binary AO algorithm versions are used to solve the feature selection issue. The feature selection challenge is a multi-objective problem that calls for the accomplishment of two opposing goals. There is a contradiction here between reducing the selection of characteristics and objectively optimising accuracy. Equation illustrates the weighted sum multi-objective fitness function for assessing each solution (18)

$$fitness = \sigma Class_{error}(F) + \tau \frac{ch\_featu}{tot\_featu}$$

where are two factors which indicates the weight of accuracy and the number of selected features and their values are set in the range of  $\sigma \in [0, 1]$  and  $\tau = 1 - \sigma$ . The classification error, the number of chosen features, and the total number of features are  $Class_{error}$ ,  $ch\_featu$ , and  $tot\_featu$ , respectively.

where  $\sigma$  and  $\tau$  are two variables with values set in the range of  $[0, 1]$  and  $\tau = 1 - \sigma$ , respectively, and reflect the weight of accuracy and the number of chosen characteristics.  $Class_{error}$ ,  $ch\_featu$ , and  $tot\_featu$  respectively, stand for the classification error, the number of selected features, and the total number of features.

### Classification using VGG-19+RESNET50

To categorise big datasets for use in decision-making, pattern detection, and other processes, data classification is a crucial component. When dealing with multi-class classification issues including classes that are mutually exclusive, a classification layer employs a fully linked layer to calculate the cross entropy loss. In this module, we rebuild the potent VGG-19+RESNET50 with fine tweaking for the network parameters and hyperparameters using the transfer learning approach. After preprocessing the acquired dataset, this is achieved by building a ResNet-50 model with pretrained parameters (weights) using the imagenet dataset (histopathologic images)

Simonyan and Zisserman (2014) proposed the VGG19, a 19-layer convolutional neural network with 16 convolutional layers and three fully connected layers, to classify the pictures into 1000 segments. The VGG19 model was trained using the ImageNet database that contains one million images organised into 1000 segments. It is a very popular method for identifying pictures since every convolutional layer has several 33 filters. The structure of VGG19+RESNET 50 is shown in Fig. 2. This illustrates that categorization is achieved using the last Three convolutional layers whereas extracted features is achieved by employing the first 16 convolutional layers. A max-pooling layer is added it after every group of the five feature extraction layer, which are separated into groups of two. This model creates the label for the object in the image after receiving a 224x224 image. In the research, features are obtained using a pre-trained VGG19 model, and various machine learning techniques are utilised for classification. Since the CNN model calculates a substantial number of variables after extracting features, image

compression is necessary to lower the size of the feature vector. With Locality Preserving Projection, the dimensionality is reduced, and then a classification approach is used.

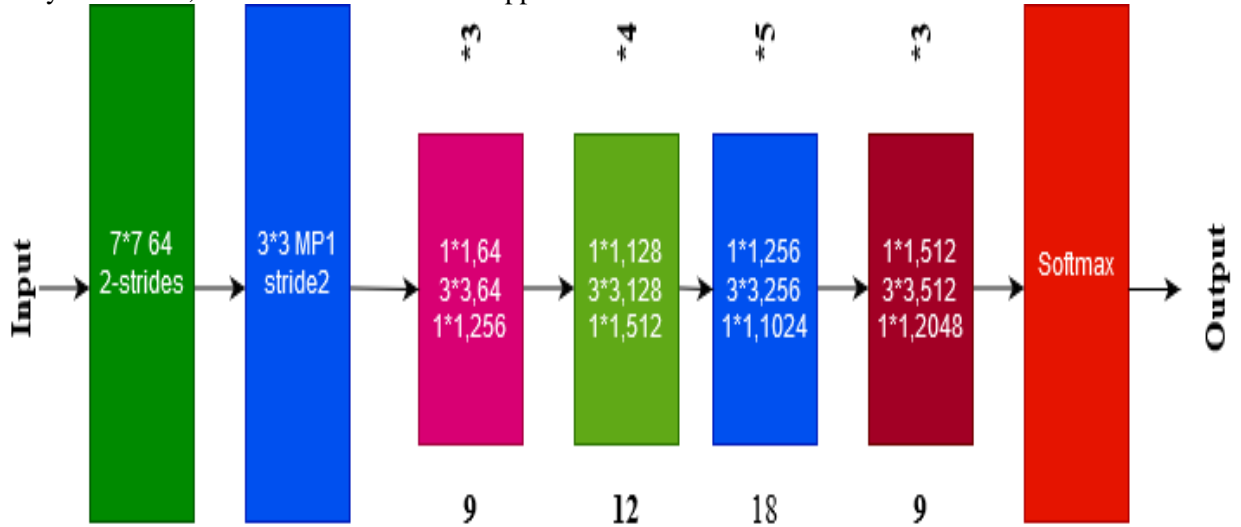


Figure-2 architecture of RESNET50

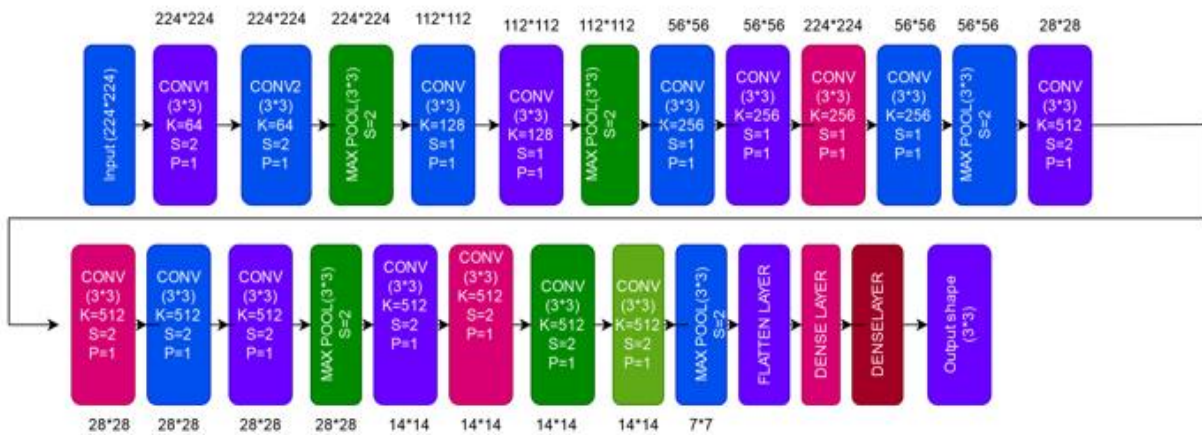


Figure-3 architecture of VGG-19

The module accepts the ResNet-50 features and passes them through a fully connected (FC) layer made up of 1024 neurons with a 40% dropout configuration to avoid over-fitting. Following that, the units' rectification function, or *ReLU*, was engaged. The *ReLU* function,  $MAX(X, 0)$ , preserves all other values fixed and sets all negative values in the matrices  $X$  to zero. *ReLU* is used because deep network training with it tends to converge considerably more rapidly and consistently than deep network training with sigmoid activation. Finally, one neuron unit equipped with the *Sigmoid* function made up the output layer, which provided the probabilities for the classes (Binary classifier). The mathematical function *Sigmoid* normalises a vector of  $K$  real values into a probability distribution made up of two probabilities (e.g. Benign vs Malignant). The following is a definition of *Sigmoid* function:

$$s(x)_i = \frac{1}{1 + e^{-x}} = \frac{e^x}{e^x + 1}, S: R^k \rightarrow R$$

For  $i = 1, 2, \dots, K$  and  $x = (x_1, x_2, \dots, x_k) \in R^k$

Additionally, we used *MeanSquaredError (MSE) loss* to compute the loss for training and testing. To calculate MSE Loss, determine the average of the squared differences between the expected and actual values. Whether the predicted and actual values are positive or negative, the result always is positive, and a correct value is 0.05. The following defines the MSE function:

$$MSE = \frac{1}{n} \sum_{i=1}^n (Y_i - Y'_i)^2$$

where  $n$  is the sample count,  $Y_i$  is the sample of raw data, and  $Y'_i$  is the sample of predicted data. Finally, we used the Root Mean Square Propagation optimizer to complete the compilation of the *Kerasmodel (RMSprop)*.

The recent gradients' magnitude is used by *RMSprop* to normalise the gradients. In *RMSprop*, For every weight, we calculate the running average of the most significant gradients' magnitudes and dividing it by the weight's learning rate. So, for every weight, keep a moving average of the squared gradient.

Step-1: preprocessing of images

Step1.1: Normalization the window level

Step 1.2: develop the radii  $r_{in}$  and  $r_{out}$

Step 1.3: reduce the noise level

Step-2: preprocessed images

Step 2.1: find the lower and upper level dimensional space [ $Low, Upp$ ]

Step 2.2: find the prey in the above determined dimension

Step 2.3: update the number of prey for various iterations

Step 2.4: initiate narrowed exploration

Step 2.5: Find the Levy flight distribution function for each prey

Step 2.6: initiate the Expanded exploitation

Step 2.7: update the fitness value

$$fitness = \sigma \text{Class}_{error}(F) + \tau \frac{ch\_featu}{tot\_featu}$$

Step 2.8: extract and select the optimal bone tumor feature

Step 3: give the extracted image to VGG-19+RESNET50

Step 3.1: pretraining process

Step 3.2 update the sigmoid activation function

Step 3.3 Classify the image

### Parameter Calculations of RESNET-50 and VGG-19 :

Table-1: RESNET-50 Parameter calculation

Parameters	Calculations	Tot. no of Parm
$(3 \times (1 \times 1) + 1)64$	256 X 3	768
$(64 \times (1 \times 1) + 1)128$	8320 X 4	33280
$(128 \times (1 \times 1) + 1)256$	33024 X 5	165120
$(256 \times (1 \times 1) + 1)572$	131584 X 3	394752
$(3 \times (3 \times 3) + 1)64$	1792 X 3	5376
$(64 \times (3 \times 3) + 1)128$	73856 X 4	295424
$(128 \times (3 \times 3) + 1)256$	33024 X 5	1475840
$(256 \times (3 \times 3) + 1)512$	131584 X 3	3457536
$(3 \times (1 \times 1) + 1)256$	1024 X 3	3072
$(256 \times (1 \times 1) + 1)512$	257 X 512	526336
$(512 \times (1 \times 1) + 1)1024$	525312 X 5	2626560



(1024 X(1X1) + 1)2048	2099200X 3	6297600
	total	15281664

Table-2:VGG-19 Parameter calculation

Layers	Output shape	Parameter
Conv1	(none,224,224,64)	1792
Conv2	(none,224,224,64)	36928
MP1	(none,112,112,64)	0
CONV3	(none,112,112,128)	73856
CONV4	(none,112,112,128)	147584
MP2	(none,56,56,256)	0
CONV5	(none,56,56,256)	295168
CONV6	(none,56,56,256)	590080
CONV7	(none,56,56,256)	590080
MP3	(none,28,28,256)	0
CONV8	(none,28,28,512)	1180160
CONV9	(none,28,28,512)	2359808
CONV10	(none,28,28,512)	2359808
<b>MP</b>	<b>(none,14,14,512)</b>	<b>0</b>
Conv11	(none,14,14,512)	2359808
CONV12	(none,14,14,512)	2359808
CONV13	(None,14,14,512)	2359808
MP	(none,7,7,512)	0
FL1	(none,25088)	0
DENSE LAYER1	(none,4096)	0
DROPOUTLAYER_1	(none,4096)	0
DENSE LAYER	(none,4096)	16781312
DROPOUT_2	(none,4096)	0

DENSE LAYER	(None,3)	8194
Total Parameters=134,268,738		
Trainable Parameters=134,268,738		

**Performance analysis:**

The evaluation of the disarray matrix relies on the evaluation of many boundaries, including exactness, correctness, review, and F1-Score. When evaluating the specified boundaries, True Positive (TP), False Negative (FN), True Negative (TN), and False Positive are considered (FP). **Accuracy:** It is described as the ratio of all values that were accurately anticipated to all predictions made according to equation (18)

$$Accuracy = \frac{TP+TN}{TP+TN+FP+FN} (18)$$

**Recall:** The exact predicted values are included in the overall anticipated values as in eq (19)

$$Recall = \frac{TP}{TP+FN} (19)$$

**Precision:** The total projected values as in eq (20) are the genuine positive values

$$Precision = \frac{TP}{TP+FP} (20)$$

**F1 - Score:** Equation (21) states that it is the ratio of average accuracy to recall

$$F1 - Score = 2 * \frac{Precision*Recall}{Precision+Recall} (21)$$

Comparison of proposed VGG-19+RESNET50 is done with the existing methods such as, Deep Convolutional Extreme Learning Machine (DC-ELM), Recurrent CONVoluted neural networks (Rec-CONVnet), EfficientNet\_CNN.

Table-3 comparison of accuracy

Numberofpochs	DC-ELM	Rec-CONVnet	EfficientNet_CNN	VGG-19+RESNET50
100	96.4	98.4	87.5	99.8
200	97.5	97.5	88	98.5
300	97.4	98.5	89.6	98.5
400	96.5	97.4	89.4	99.4
500	96.5	97	87	99

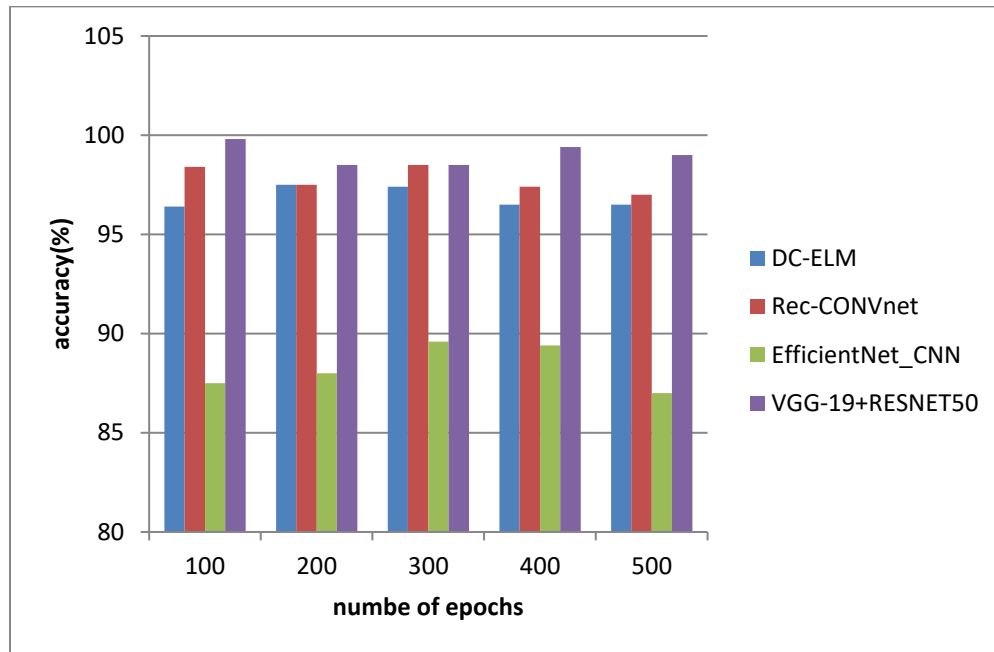


Figure 4: comparison of accuracy

The accuracy of the suggested VGG-19+RESNET50 technique is compared to that of the existing DC-ELM, Rec-CONVnet, and EfficientNet CNN methods in Figure 3. The number of epochs and accuracy values achieved in % are shown on the X and Y axes, accordingly. Contrastedly, the suggested technique obtains 99.7%, which is 2.50%, 1.43%, and 10.5% better than the aforementioned existing methods, which reach 97.27%, 98.34%, and 89.2%.

Table-4 comparison of precision

Number of epochs	DC-ELM	Rec-CONVnet	EfficientNet_CNN	VGG-19+RESNET50
100	87.5	97.1	90.2	98.2
200	86.9	98.3	89.4	97.6
300	87	97.4	89.4	98
400	86.9	97.6	90.3	97.5
500	84	98	90	98.3

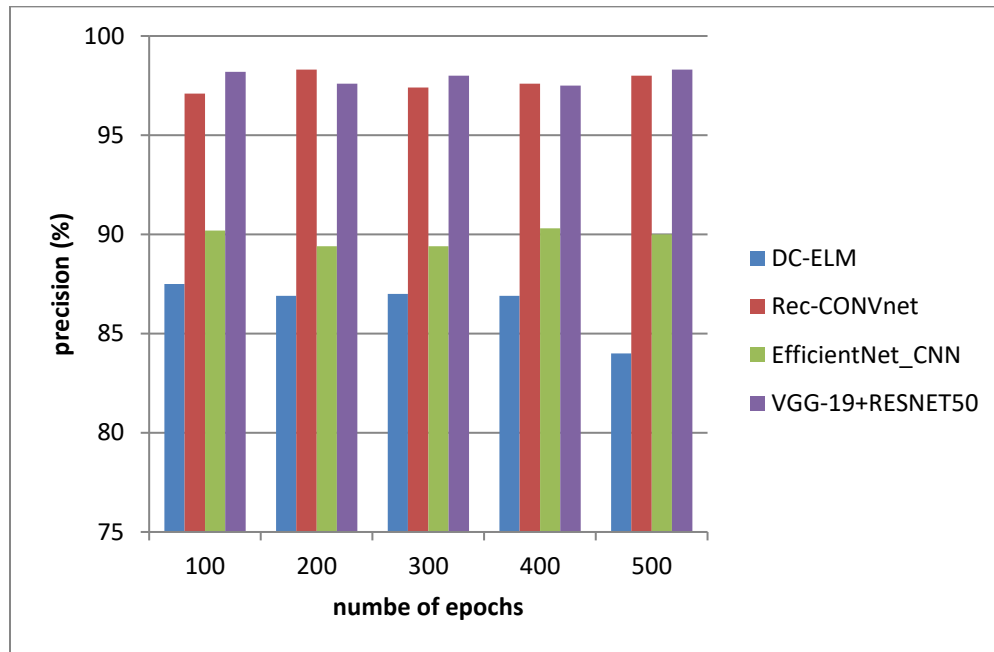


Figure 5: comparison of precision

Figure 4 compares the suggested VGG-19+RESNET50 method's accuracy to that of the existing DC-ELM, Rec-CONVnet, and EfficientNet\_CNN methods. The number of epochs and the accuracy values achieved in % are shown on the X and Y axes, correspondingly. Comparatively, the suggested technique obtains 98.8%, which is 11%, 1.26%, and 8.8% better than the aforementioned existing methods, which obtain 87.832%, 97.96%, and 90%.

Table-5 comparison of recall

Number of epochs	DC-ELM	Rec-CONVnet	EfficientNet_CNN	VGG-19+RESNET50
100	98	98	80.5	99.2
200	97.6	97.1	79.4	99.5
300	98.4	98.5	79.6	99.3
400	98	98.4	80.5	99.3
500	97.3	97.6	80.4	99.6

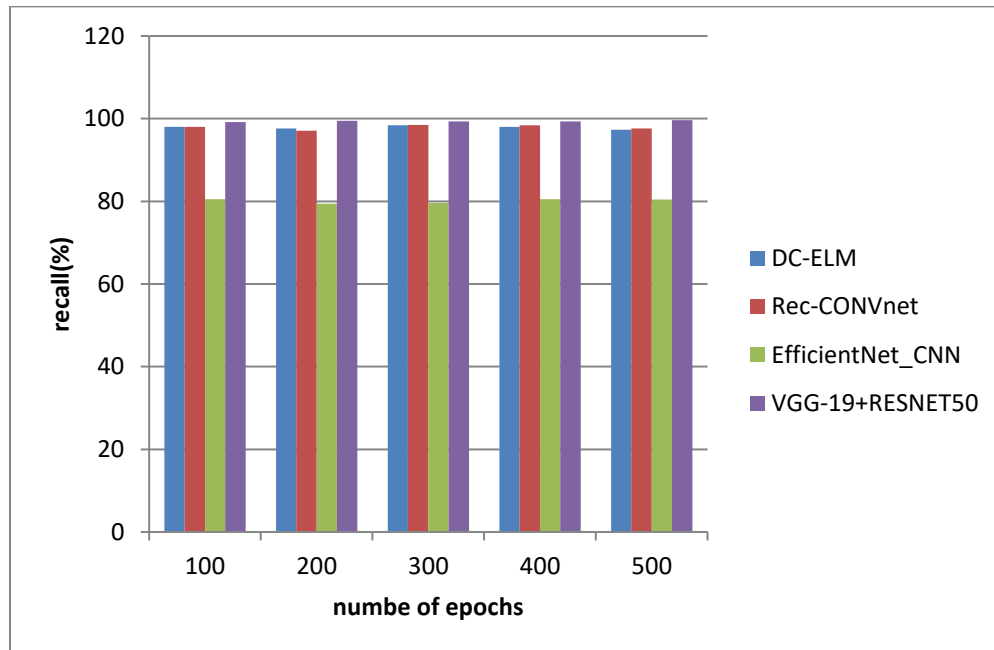


Figure 6: comparison of recall

Figure 5 compares the suggested VGG-19+RESNET50 approach with the recall of the conventional DC-ELM, Rec-CONVnet, and EfficientNet CNN methods. The number of epochs and the recall values acquired in % are shown on the X and Y axes, correspondingly. Comparatively, the suggested technique obtains 99.2%, which is 1%, 1.2%, and 20% better than the aforementioned conventional systems, which obtain 98.204%, 98.72%, and 80%.

Table-6 comparison of F1 measure

Number epochs	of	DC-ELM	Rec-CONVnet	EfficientNet_CNN	VGG-19+RESNET50
100		97	98.7	77.6	99.2
200		96.5	97.6	78.8	99.5
300		97.5	95.7	79.6	99.3
400		96	98.6	77.8	99.3
500		96.7	97.5	77	99.6

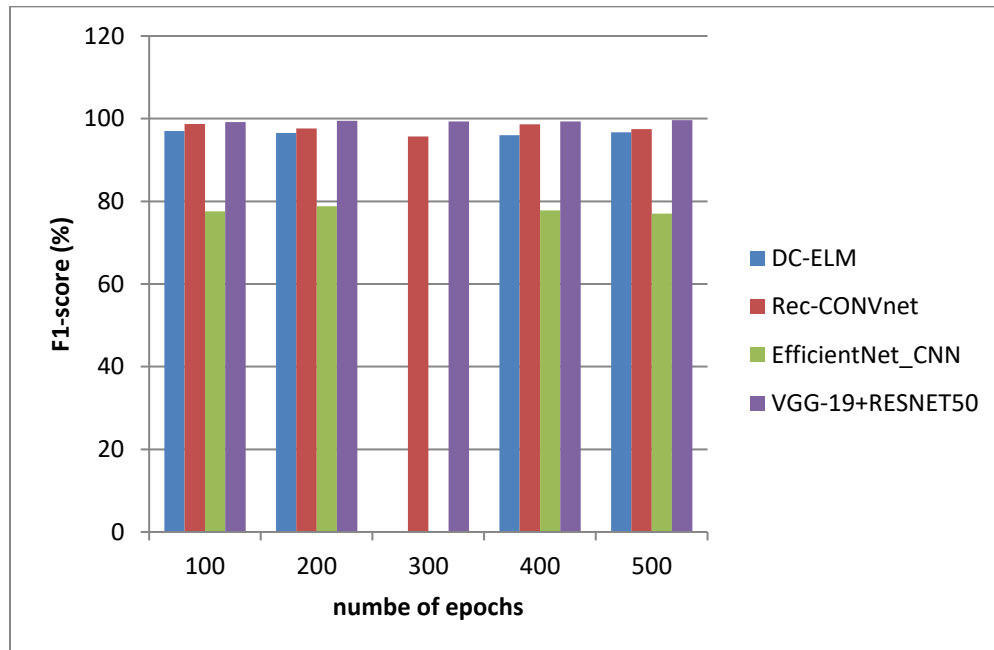


Figure 7: comparison of F1 measure

The F1-score of the existing DC-ELM, Rec-CONVnet, EfficientNet CNN, and the suggested VGG-19+RESNET50 approach is shown in Figure 6. The X axis and Y axis, respectively, display the number of epochs and the F1-score values attained in %. When contrasted, the suggested technique obtains 99.3%, which is 1%, 1.2%, and 20% better than the aforementioned existing methods, which obtain 97.2%, 98.32%, and 77.6%, respectively.

Table-7 Overall comparative analysis

Parameters	DC-ELM	Rec-CONVnet	EfficientNet_CNN	VGG-19+RESNET50
Accuracy	97.27	98.34	89.2	99.7
Precision	87.832	97.96	90	98.8
Recall	98.204	98.72	80	99.2
F1-score	97.2	98.32	77.6	99.3

**Conclusion**

Automating the categorization of histology images by computer-aided systems is crucial in the field of medical image processing. The process of doing a microscopic analysis of histological pictures is time-consuming and complicated. Histology is automatically diagnosed, which reduces labour and frees pathologists to concentrate on challenging cases. VGG19 and RESNET50, two pre-trained networks from the Keras toolkit, were employed in this study. To prevent variance, regularisation and optimization approaches were used.

**Reference**

1. S. Jeong, W. Kim, B. Byun, C.-B. Kong, W. Song, I. Lim, S. Lim, and S.-K. Woo, “Prediction of chemotherapy response of osteosarcoma using baseline 18 f-fdg textural features machine learning approaches with pca,” Contrast Media Molecular Imaging, vol. 2019, pp. 1-7, July 2019.
2. M. Smith, S. Altekruse, P. Adamson, G. Reaman, and N. Seibel, “Declining childhood and adolescent cancer mortality,” Cancer, vol. 120, Aug 2014.
3. Z. Li, S. M. R. Soroushmehr, Y. Hua, M. Mao, Y. Qiu, and K. Najarian, “Classifying osteosarcoma patients using machine learning approaches,” in 2017 39th Annual International Conference of the IEEE Engineering in Medicine and Biology Society (EMBC), 2017, pp. 82-85.

4. R. Mandava, O. Alia, C.-W. Bong, D. Ramachandram, M. Aziz, and I. L. Shuaib, "Osteosarcoma segmentation in mri using dynamic harmony search based clustering," Dec 2010, pp. 423-429.
5. M. L. Rahman, R. Arman Nabid, and M. F. Hossain, "Disease symptom analysis based department selection using machine learning for medical treatment," in 2020 IEEE International Students' Conference on Electrical, Electronics and Computer Science (SCEECS), 2020, pp. 1-5
6. K. Munir, H. Elahi, A. Ayub, F. Frezza, and A. Rizzi, "cancers cancer diagnosis using deep learning: A bibliographic review," *Cancers*, vol. 11, Aug 2019.
7. M. D'Acunto, M. Martinelli, and D. Moroni, "From human mesenchymal stromal cells to osteosarcoma cells classification by deep learning," *Journal of Intelligent Fuzzy Systems*, vol. 37, pp. 1-8, July 2019.
8. Ahmed, U. Prediction of Diabetes Empowered with Fused Machine Learning. *IEEE Access* 2022, 10, 8529–8538. [CrossRef]
9. Nasir, M.U.; Khan, M.A.; Zubair, M.; Ghazal, T.M.; Said, R.A.; Al Hamadi, H. Single and mitochondrial gene inheritance disorder prediction using machine learning. *Comput. Mater. Contin.* 2022, 73, 954–963.
10. Rahman, A.U.; Alqahtani, A.; Aldhaffer, N.; Nasir, M.U.; Khan, M.F.; Khan, M.A.; Mosavi, A. Histopathologic Oral Cancer Prediction Using Oral Squamous Cell Carcinoma Biopsy Empowered with Transfer Learning. *Sensors* 2022, 22, 3833.
11. Bansal, P.; Kumar, S.; Srivastava, R.; Agarwal, S. Using transfer learning and hierarchical classifier to diagnose melanoma from dermoscopic images. *Int. J. Healthc. Inf. Syst. Inform. (IJHISI)* 2021, 16, 73–86. [CrossRef]
12. Bisla, D.; Choromanska, A.; Berman, R.S.; Stein, J.A.; Polsky, D. Towards automated melanoma detection with deep learning: Data purification and augmentation. In *Proceedings of the IEEE/CVF Conference on Computer Vision and Pattern Recognition Workshops, Long Beach, CA, USA, 16–17 June 2019*; pp. 2720–2728.
13. Cao, Z.; Duan, L.; Yang, G. An experimental study on breast lesion detection and classification from ultrasound images using deep learning architectures. *BMC Med. Imaging* 2019, 19, 51
14. Sharma, A., Yadav, D. P., Garg, H., Kumar, M., Sharma, B., & Koundal, D. (2021). Bone cancer detection using feature extraction based machine learning model. *Computational and Mathematical Methods in Medicine, 2021*.
15. Mishra, R., Daescu, O., Leavey, P., Rakheja, D., & Sengupta, A. (2017, May). Histopathological diagnosis for viable and non-viable tumor prediction for osteosarcoma using convolutional neural network. In *International Symposium on Bioinformatics Research and Applications* (pp. 12-23). Springer, Cham.
16. Anand, D., Arulselvi, G., Balaji, G. N., & Chandra, G. R. (2022). A Deep Convolutional Extreme Machine Learning Classification Method to Detect Bone Cancer from Histopathological Images. *International Journal of Intelligent Systems and Applications in Engineering, 10(4)*, 39-47.
17. von Schacky, C. E., Wilhelm, N. J., Schäfer, V. S., Leonhardt, Y., Gassert, F. G., Foreman, S. C., ... & Gersing, A. S. (2021). Multitask deep learning for segmentation and classification of primary bone tumors on radiographs. *Radiology, 301(2)*, 398-406.
18. Tang, H., Sun, N., & Shen, S. (2021). Improving generalization of deep learning models for diagnostic pathology by increasing variability in training data: Experiments on osteosarcoma subtypes. *Journal of Pathology Informatics, 12(1)*, 30.
19. Arunachalam, H. B., Mishra, R., Daescu, O., Cederberg, K., Rakheja, D., Sengupta, A., ... & Leavey, P. (2019). Viable and necrotic tumor assessment from whole slide images of osteosarcoma using machine-learning and deep-learning models. *PloS one, 14(4)*, e0210706.
20. Brück, O. E., Lallukka-Brück, S. E., Hohtari, H. R., Ianevski, A., Ebeling, F. T., Kovanen, P. E., ... & Mustjoki, S. M. (2021). Machine Learning of Bone Marrow Histopathology Identifies Genetic and Clinical Determinants in Patients with MDS Histopathologic Landscape of MDS. *Blood cancer discovery, 2(3)*, 238-249.